

# APPLICATION OF PERMANENT MAGNET BIAS MAGNETIC BEARINGS TO AN ENERGY STORAGE FLYWHEEL

Lawrence A. Hawkins  
CalNetix, Inc.  
Torrance, CA 90501

Brian T. Murphy  
John Kajs  
Center for Electromechanics  
University of Texas  
Austin, TX 78712

## ABSTRACT

The design and initial testing of a five axis magnetic bearing system in an energy storage flywheel is presented. The flywheel is under development at the University of Texas Center for Electromechanics (UT-CEM) for application in a transit bus. CalNetix performed the system dynamic analysis, developed the magnetic bearing control algorithms, and developed the digital control hardware to meet the needs of the flywheel system. The bearing system for the prototype features two types of homopolar, permanent magnet bias magnetic bearings: a combination radial/thrust bearing and a pure radial bearing. The backup bearing system features a viscously damped, compliant mount. The system has been successfully tested to the maximum design speed of 42,000 rpm. A gain-scheduled, MIMO control algorithm was required to control the system modes affected by rotor gyroscopics. The implementation and basis for this control scheme is discussed. Dynamic test results are discussed relative to the rotordynamic and control system design.

## INTRODUCTION

UT-CEM is developing a flywheel energy storage system, conveniently referred to as a flywheel battery (FWB), for use in a power-averaging role in a hybrid electric bus [1,2]. Energy generated during vehicle braking is converted to mechanical energy by using a motor/generator to drive the FWB. During vehicle acceleration, the motor/generator extracts energy from the FWB, completing the storage/recovery cycle. FWBs are ideal for this application because they have significantly higher power densities and longer life than other types of batteries [3]. The system, shown in Figure 1, is designed to store 2 kWh at 40,000 rpm, and produce 110 kW of continuous power (150 kW peak).

The goal of maximizing energy density leads to carbon fiber composites as the material of choice for modern high performance flywheels. These materials can operate safely at surface speeds of 1,000 m/s, as opposed to only 200-300 m/s for metals. The high surface speeds result in unacceptable windage losses unless the rotor operates in a vacuum. Thus rotor heat removal must be accomplished through radiation, making minimization of rotor heating a major design consideration. Consequently, low-loss homopolar, permanent magnet bias magnetic bearings and a permanent magnet motor/generator were chosen to reduce rotor heating. Initial testing was performed with a titanium flywheel rotor having a 9.9 inch outer diameter. This allowed for safe evaluation of the magnetic bearings and motor/generator. Now that the bearings and motor/generator are fully functional, complete thermal testing is underway. When thermal tests are complete, the titanium rotor will be machined down and composite rings added to bring the outer diameter up to 17.5 inches. This change to the rotor will alter its weight and polar-to-transverse inertia ratio,  $I_p/I_t$ . At that time the magnetic bearing control algorithms will require additional refinement for the reconfigured rotor.

In order to achieve the target operating speed, a gain scheduled MIMO control approach was developed. Similar approaches have been applied to magnetic bearings for other applications [4,5]. These features were applied in a limited way for the current system with titanium flywheel. Future testing of the composite flywheel will probably require additional sophistication, such as that provided by the more recent Linear Parameters Varying (LPV) approach [6,7].

## FLYWHEEL BATTERY

The vertically mounted flywheel battery (Figure 1) uses a pancake flywheel placed below a separate motor/generator on the same shaft. This partially integrated configuration was chosen to allow integration of an existing, proven motor/generator with a robust flywheel design [1]. Although the composite flywheel section has a high  $I_p/I_t$ , the rigid body  $I_p/I_t$  for the entire flywheel rotor is significantly less than 1.0 (0.45 for the rotor in Figure 1) due to the size of the high-power density motor/generator. The motor/generator utilizes a diametrically polarized permanent magnet rotor (two pole) designed by AlliedSignal Aerospace. The magnet is captured radially by a thick inconel sleeve, which also provides the structural connection to the rest of the flywheel rotor. A beryllium copper sleeve is shrunk over the inconel sleeve to reduce rotor eddy current losses. The three phase, two pole toothless stator is ring wound with non-potted Litz wire, allowing minimum end turn length and excellent flow-through liquid cooling of the stator winding.

The magnetic bearings are placed immediately above the motor/generator and immediately below the flywheel. Rolling element backup bearings are placed outboard of the magnetic bearings. The magnetic bearings are inboard of the backup bearings for two distinct reasons: 1) this is the best bearing location from a rotordynamic standpoint, and since the backup bearings are intended for use only during rare events (preferably never)

they are naturally placed in a less optimal location, and 2) the backup bearings are not capable of operation at the same high surface speeds as the magnetic bearings, so they are placed outboard where the shaft diameter can be reduced to lower the surface speed.

### Magnetic Bearing

The magnetic bearings use a homopolar, permanent magnet bias topology. Homopolar refers to the direction of the bias flux, which is oriented either uniformly into or uniformly out of the shaft at any circumferential location. This topology significantly reduces rotor eddy current losses compared to conventional designs. A permanent magnet is used to produce the bias flux for the bearing, resulting in several advantages compared to electromagnetic bias: 1) less power is consumed by the magnetic bearings, 2) the bearing has a more linear force/displacement characteristic due to the contribution of the large, fixed reluctance of the permanent magnet to the bias flux path, and 3) only one amplifier is required per axis, increasing reliability and reducing cost compared to conventional designs that use two amplifiers per axis.

The combo bearing in Figure 1 is a three-axis combination radial/thrust bearing. A combination bearing is more compact axially than separate radial and axial magnetic bearings. This increases the frequency of the rotor bending modes, making the magnetic bearing control design less difficult. This combination bearing, shown in more detail in Figure 2, uses a single radially polarized permanent magnet ring to provide bias flux for both the radial and axial flux paths. Three separate pairs of control coils allow individual control of each axis (two radial and one axial).

The radial (Brg 2) bearing is a two-axis radial bearing. The basic operation of this bearing was described in [8]. Some characteristics of the magnetic bearings are given in Table 1.

**Table 1. Magnetic Bearing Characteristics.**

Bearing	Combo Bearing (Radial)	Radial Bearing	Combo Bearing (Axial)
Bearing Reference Name	Brg 1	Brg 2	Thrust
Channel Names	1,2	3,4	5
Coordinate Names	x1,y1	x2,y2	Z
Load Capacity, N (lbf)	1115 (250)	670 (150)	2230 (500)
Force Constant, N/A (lbf/A)	156 (35)	94 (21)	303 (68)
Negative Stiffness, N/mm (lbf/in)	1751 (10,000)	963(5500)	3502 (20,000)
Air Gap, mm (in)	0.508 (.020)	0.508 (.020)	0.508 (.020)
Maximum Current, A	7.1	7.1	7.4

### Backup Bearings

The backup bearings have radial and axial clearances of 0.010 inches (one-half of the magnetic air gap) between the bearing inner races and the shaft. The backup bearings are

expected to carry load in the following cases: 1) when the system is at rest and the magnetic bearings are turned off, 2) in the event of a substantial shock transient that exceeds the capacity of the magnetic bearings, and 3) in the event of a component failure that causes the loss of one more axes of control for the magnetic bearing.

The backup bearing system consists of a duplex pair of angular contact ball bearings at each end of the shaft. The lower backup bearing also acts as a backup thrust bearing due to the inclusion of thrust collars on the rotor. The bearing materials are 440C inner and outer races, SiN<sub>3</sub> balls, composite cage, and dry film lube (MoS<sub>2</sub>). Leaded bronze sleeves are used for the rotor contacting surfaces. This material provides a touchdown surface with low friction characteristics at the expense of long wear life.

A radially compliant backup bearing support in parallel with a sealed viscous damper contains the backup bearings. The nominal stiffness and damping characteristics selected for the support were 100,000 lb/in and 150 lb-s/in respectively. These values were defined by a parametric study using a transient, nonlinear drop and spin down rotordynamic analysis. The selection criteria were to minimize deflection and load during critical speed traverse on the spin down, and to minimize static deflection and load during drop impact transient and at rest.

## SYSTEM MODELLING

### Rotordynamic Model

The rotordynamic structural model is shown in Figure 3. The top half shows the stiffness model and the lower half the mass model. The actuator and sensor locations and the first free/free, zero-speed bending mode are superimposed on the plot. Notice that the sensor and actuator modal displacements are lower at Brg 1 compared to Brg 2 in the first bending mode. The first four bending modes are included in the system analysis. The frequencies of those modes at zero speed are: 745 hz, 1425 hz, 1990 hz, and 3590 hz.

The rotordynamic equation of motion for the plant, which is in general a coupled, flexible rotor/casing system with conventional bearings, is:

$$[M]\{\ddot{q}\} + [C]\{\dot{q}\} + [K]\{q\} = \{f\} \quad (1)$$

Where  $q$  represents the physical coordinate degrees of freedom,  $f$  represents external forces, and the mass matrix is represented by  $\mathbf{M}$ . The passive negative stiffness of the magnetic bearing is included in the bearing stiffness matrix,  $\mathbf{K}$ . The terms representing gyroscopic effects are part of the rotor partition of the damping matrix,  $\mathbf{C}$ .

For the flywheel, each rotor bending mode was given a static internal damping ratio,  $\hat{\imath}_{ns}=0.5\%$ . This is a reasonable value for a rotor with sleeves if no modal test data is

available. The dynamic internal damping for rotor modes is reduced as speed increases by:

$$\mathbf{x}_n = \mathbf{x}_{ns} \left( \frac{\omega_n - \omega_{spin}}{\omega_n} \right) \quad (2)$$

Where  $\omega_n$  represents the natural frequency of the mode, and  $\omega_{spin}$  represents the spin frequency. The basis for this circular whirl approximation can be derived from the discussion of internal rotor damping by Childs [9].

For system analysis with magnetic bearings, the plant represented by Eqn. (1) is transformed to modal coordinates,  $\mu$ , and converted to state space form:

$$\begin{aligned} \{\dot{\mathbf{m}}_p\} &= [A_p] \{\mathbf{m}_p\} + [B_p] \{f\} \\ \{q\} &= [C_p] \{\mathbf{m}_p\} + [D_p] \{f\} \end{aligned} \quad (3)$$

Partitions of the characteristic matrix  $\mathbf{A}_p$  contain the modal stiffness and damping matrices. The input and output matrices  $\mathbf{B}_p$  and  $\mathbf{C}_p$  contain mass normalized eigenvectors for modes selected for the system analysis. Some authors include the passive negative stiffness as part of the feed forward matrix  $\mathbf{D}_p$  instead of as a bearing stiffness in  $\mathbf{K}$ . These equations have been presented in detail by several authors; one recent example is Antkowiak [10].

Predicted and measured plant bode plots are shown in Figure 4 for zero speed. Both curves include the bearing and sensor dynamics because the plant must be measured in the installed system by taking the transfer function between the position sensor and the amplifier current monitor. The phase roll-off seen in Figure 4 beginning around 100 hz is due to the low pass filter (bandwidth of 3.4 kHz) in the position sensor demodulation electronics. The weak mode at about 30 hz in the measured transfer function is the rigid body mode of the system on the elastomeric housing supports. Due to its limited influence on the control of the rotor, the housing was not included as part of the plant model for this stage of the FWB analysis. Future application of this FWB to the transit bus platform will require inclusion of the housing and gimbal dynamics in the system model. Although the coherence of the measured result is poor above 800 hz, the first two bending modes at 750 and 1425 hz are apparent and consistent with model predictions.

### System Analysis

The initial magnetic bearing transfer function for Brg 1 (x1 and y1) is given in Figure 5. The transfer function for Brg 2 is similar. For linear response and eigenvalues analysis, the magnetic bearing transfer functions are converted to state space form and coupled to the plant model of Eqn. (3). Figure 6 is a comparison of the predicted versus measured closed loop transfer function of the system. Overall, the agreement is reasonable; however, the predicted damping is somewhat high near the rigid body mode at about 150 hz. Again, the measurement coherence is poor above about 800 hz. Figure 7 is a plot of all predicted system natural frequencies below 1000 hz that have damping ratios ( $\xi$ ) less

than 0.25. Well damped modes were left out because the large number of such modes in the system make this type of plot difficult to interpret. The strong gyroscopic influence is responsible for the rise of the second rotor rigid body mode with speed, as well as the spread of the forward and backward bending modes (see Figure 7).

## CONTROL SYSTEM DEVELOPMENT

### Speed Independent, SISO Control Approach

The original magnetic bearing system was designed and built by Avcon, a company that ceased operation just as the flywheel was initially assembled. Due to limited processing power of the DSP in the controller supplied with the system, the original control hardware allowed only SISO compensation with a maximum of six biquad filters per axis at a 10 kHz sample rate. No speed input was provided, thus a successful compensation would have to control all modes of the system from rest to 42,000 rpm. This task is readily achievable for some types of rotors; but not practical for a rotor with substantial gyroscopic effects such as this FWB. Stability of the rigid body conical mode and/or the backward first bending mode was marginal at all speeds above 30,000 rpm. The highest speed achieved with the SISO single speed controller was 37,000 rpm.

The SISO transfer function was shown in Figure 5. The control strategy used was to provide direct phase lead for the second rigid body mode, roll off the compensation quickly enough to again provide phase lead for the backward and forward components of the first bending mode. The backward bending mode needed phase lead throughout the operating range. However, the forward bending mode exits the positive phase lead region near 900 hz. The mode is still stable due to the low gain of the transfer function at those frequencies. This strategy has a limit in that at higher speeds, the frequencies of the forward rigid body mode and the first backward bending mode become close enough that the phase cannot be transitioned quickly enough between the modes. That limit was reached at 37,000 rpm for this rotor and the original control hardware.

### Gain Scheduled, MIMO Control Approach

#### Hardware Development

In order to bring the machine to full speed operation, CalNetix developed a new stand-alone control module based on the Texas Instruments TMS 320C6201 (C6x) digital signal processor (DSP). This control module provided a factor of 5 to 10 increase in processing speed, program memory and data memory. Whereas, the previous control module had to be programmed in assembly and used 80  $\mu$ s (80% of available processing time at a 10 kHz sample rate) to execute the desired set of transfer functions for the flywheel (a 12 state compensator for each radial axis, 4 states for the axial), the new control module could execute the same set of transfer functions in about 15  $\mu$ s with a

control program written in C. Since a 10 kHz sample rate is suitable for most magnetic bearing supported turbomachinery, the new control hardware comfortably allows at least five times as many instructions as the previous hardware. The new control hardware also allowed the easy incorporation of a speed/phase detection scheme. Thus previously unavailable MIMO and gain scheduled control schemes could now be used.

### Gain Scheduling Implementation

As an initial implementation of gain scheduled control, the control program was structured to access up to four independent sets of control parameters (filter coefficients and gains). Each set of control parameters is applied in a different rotor spin speed range. The speed ranges overlap so that the selected set of control parameters is prevented from toggling back and forth near a transition speed. The speed ranges for the FWB are indicated on the natural frequency map of Figure 7. When the spin speed moves into a new speed range, the coefficients for that speed range are made current. This feature allows the use of a transfer function that is optimized more closely to the plant requirements within a given speed range than can be accomplished with a single control structure. The choice of four speed ranges was made simply to address the (now) well-known needs of the titanium FWB. The only hard limit to the number of speed ranges imposed by the control module is the amount of data memory used, which is about 1 kB per speed range with the structure now in use. Since robust operation had been achieved to 30,000 rpm with a single set of control parameters, the initial implementation of gain scheduling focused on simple modifications to this compensation. Parameters for the first speed range were modified to provide more damping at the rigid body critical speeds. The resulting damping ratios were approximately: 0.38 and 0.32 respectively. The control parameters for the three higher speed ranges successively track the second forward rigid body mode and first backward bending mode, at the expense of reduced damping at 50-150 hz since the critical speeds have already been traversed.

### Circumferential Cross-Coupling (MIMO) Implementation

In order to further improve the damping ratios of the troublesome modes, a simple MIMO control feature was added to the control program. For the test results presented in this paper, the MIMO feature was used only for the fourth speed range, but it can easily be used in any or all speed ranges as desired. As with the SISO controller, the magnetic bearing control commands are calculated from a series of cascaded biquad filters that produce the desired transfer functions. Five direct axis transfer functions are used to represent the normal SISO control for a five-axis system. SISO implies that each axis is controlled independently of the others. In the MIMO implementation employed here, up to four additional transfer functions are provided which can be used with independently selectable input and output axes. The intended use for this feature is for circumferential (x,y) cross-coupling; however, the selection of input and output channels is general, allowing this feature to be used in other ways.

## Description of Circumferential Cross-Coupling

Circumferential cross-coupling is well suited to the flywheel because it allows the application of a phase lead to a specific region of the frequency spectrum with less influence on other parts of the spectrum. The forces that are applied by the cross-coupled terms can be understood in the following way. Consider a radial bearing to have two orthogonal axes,  $x$  and  $y$ . In a SISO controlled magnetic bearing, the bearing reaction force,  $F$ , along a given axis is due to motion only along that same axis. That is, if the rotor moves in the  $x$  axis direction, this produces a bearing force along only the  $x$  axis. This is illustrated in Eqn. (4):

$$\begin{Bmatrix} F_x \\ F_y \end{Bmatrix} = - \begin{bmatrix} H_{xx} & 0 \\ 0 & H_{yy} \end{bmatrix} \begin{Bmatrix} x \\ y \end{Bmatrix} \quad (4)$$

For magnetic bearings, the  $H$  are called transfer functions, and are generally functions of frequency. The frequency dependence in a magnetic bearing is defined by the control compensation in conjunction with the dynamic characteristics of other parts of the system such as the position sensor, power amplifier, and magnetic actuator. In a MIMO controlled magnetic bearing, the off-diagonal terms can be nonzero. This is called *circumferential* cross-coupling since the  $x$  and  $y$  axes within one radial bearing are being coupled. In this case, motion in one axis, say  $x$ , produces forces in *both* the  $x$  and  $y$  axes. This is illustrated in Eqn. (5):

$$\begin{Bmatrix} F_x \\ F_y \end{Bmatrix} = - \begin{bmatrix} H_{xx} & H_{xy} \\ H_{yx} & H_{yy} \end{bmatrix} \begin{Bmatrix} x \\ y \end{Bmatrix} \quad (5)$$

The  $H_{xy}$  and  $H_{yx}$  are the circumferential cross-coupling transfer functions. Another potentially attractive type of cross-coupling would be between the  $x$  axes (or  $y$  axes) of two radial bearings working in tandem to support a rotor.

Two of the four cross-coupled transfer functions used for the FWB are given in Figures 9 - 10. Both of these transfer functions include the dynamics of the position sensor, amplifier and magnetic actuator, and a Pade approximation of the calculation phase delay. These elements are part of the magnetic bearing transfer function. Figure 9 is the transfer function between input 2 and output 1 ( $H_{xy}$  for Brg 1). The transfer function between input 1 and output 2 ( $H_{yx}$  for Brg 1) is the same except that the gain term carries the opposite sign, making the phase different by  $180^\circ$ . The phase inversion between the two cross-coupled transfer functions is necessary to produce consistent forces at the two axes (either both leading or both lagging). Together with the opposite signed  $H_{yx}$ , the transfer function of Figure 9 produces a stabilizing force on forward modes (and a destabilizing force on backward modes) with frequencies up to about 300 hz (21,000 cpm). For modes above 300 Hz, the force is destabilizing for forward modes and stabilizing for backward modes.

The Figure 10 is the transfer function between input 4 and output 3 ( $H_{xy}$  for Brg 2).  $H_{yx}$  for Brg 2 is the same as  $H_{xy}$  except that, again, the gain term carries the opposite sign, making the phase different by  $180^\circ$ . The cross-coupled transfer function applied at Brg 2 is designed specifically to provide a stabilizing force for the first backward bending mode of the rotor, which is near 30,000 cpm when the rotor speed is in the range of 35,000 to 42,000 rpm.

## DYNAMIC TEST DATA

Figures 11 - 13 show dynamic data collected from a full-speed rundown of the machine. During rundown, the motor/generator is used to decelerate the rotor from 42,000 rpm to rest in approximately 90 seconds. Figure 11 is a plot of synchronous displacements taken from the magnetic bearing position sensors during the spin-down. There is a spike at about 1,500 rpm on all sensors due to the traverse of the housing support mode. A significant displacement at Brg 2 occurred near the expected traverse of the second rotor rigid body mode at 8,000 rpm. There is also significant displacement at Brg 1, near the traverse of a lightly damped system mode at 15,000 - 18,000 rpm. This mode is closely related to the second rigid body mode and the compensator pole that provides phase lead for the mode. These response peaks agree well with the mode locations in Figure 7. The synchronous displacements also begin to rise again between 30,000 and 42,000 rpm as the net direct stiffness of the bearing falls. Figure 12 is a plot of synchronous coil current for each bearing. The magnetic bearing control current diminishes between 30,000 and 42,000 rpm in tandem with the rise in rotor displacements. This is because the stiffness (gain) of the bearing transfer function drops significantly in this frequency range (see Figure 5). Note that the current curves exhibit steps at 24,000, 30,000, and 35,000 rpm. These are the switching points for the gain scheduling when the rotor is spinning down in speed.

A waterfall plot for the  $X1$  axis (Brg 1, input 1) position sensor is shown in Figure 13. The waterfall shows the frequency spectrum for a large number of spin speeds during the spin down from 42,000 rpm to 5,000 rpm. Two decades of the amplitude spectrum are shown, and the clearly dominant signal is the rotor synchronous displacement (700 hz at 42,000 rpm). The forward and backward bending modes are intermittently visible; at approximately 560 hz and 920 hz at 42,000 rpm, converging to 750 hz at low speed. The mode visible near 250 hz (42,000 rpm spin speed) is the second rigid body mode. This mode drops to about 150 hz at rest. The locations of these modes are in agreement with the predicted natural frequencies in Figure 7. The speed independent response at 720 hz is a noise frequency.

## CONCLUSION

System development and analysis of a permanent magnet bias, magnetic bearing system for an energy storage flywheel was described. Development and implementation of a gain-scheduled, MIMO digital control scheme was discussed. Because the needs of the

test flywheel system were moderate, the new control features have been applied in only a limited way to date. The capability of the control system will be more fully utilized in the future application to the composite rotor flywheel. Dynamic test data from full speed testing of the system showed good performance from the bearings and control system. Good agreement was found between the system analysis and test data.

## REFERENCES

1. Hayes, R.J., Kajs, J.P., Thompson, R.C., Beno, J.H., "Design and Testing of a Flywheel Battery for a Transit Bus", SAE 1999-01-1159, 1998.
2. Murphy, B.T., Beno, J.H., Bresie, D.A. "Bearing Loads in a Vehicular Flywheel Battery", PR-224, SAE Int. Congress and Exp., Detroit, 1997.
3. Reiner, G., "Experiences with the Magnetodynamic (Flywheel) storage System (MDS) in Diesel Electric and Trolley Busses in Public Transport Service," Pres. at Flywheel Energy Storage Technology Workshop, Oak Ridge, TN, 1993.
4. Matsumura, F., Namerikawa, T., Hagiwara, K., and Fujita, M., "Application of Gain Scheduled  $H_{\infty}$  Robust Controllers to a Magnetic Bearing," IEEE Transactions on Control Systems Technology, Vol. 4, no. 5, pp. 484-492, 1996.
5. Sivrioglu, S. and Nonami, K., "LMI Approach to Gain Scheduled  $H_{\infty}$  Control Beyond PID Control for Gyroscopic Rotor-Magnetic Bearing Systems," Proc. 35th Conf. On Decision and Control, pp. 3694-3699, Kobe, Japan, 1996.
7. Tsiotras, P. and Knospe, C., "Reducing Conservatism for Gain-Scheduled  $H_{\infty}$  Controllers for AMB's", Proc. of MAG'97, p. 290-299, Alexandria, VA, 1997.
6. Apkarian, P. and Adams, R.J., "Advanced Gain-Scheduling Techniques for Uncertain Systems," IEEE Transactions on Control Systems Technology, Vol. 6, no. 1, pp. 21-32, 1997.
8. Meeks, C.R., DiRusso, E., Brown, G.V., "Development of a Compact, Light Weight Magnetic Bearing", AIAA/SAE/ASME/ASEE 26th Joint Propulsion Conference, Orlando, 1990.
9. Childs, D.W., "Turbomachinery Rotordynamics", J. Wiley, New York, p. 25, 1993.
10. Ankowiak, B.M., Nelson, F.C., "Rotordynamic Modeling of An Actively Controlled Magnetic Bearing Gas Turbine Engine", ASME 97-GT-13, 1997 IGTI Turbo-Expo, Orlando, 1997.

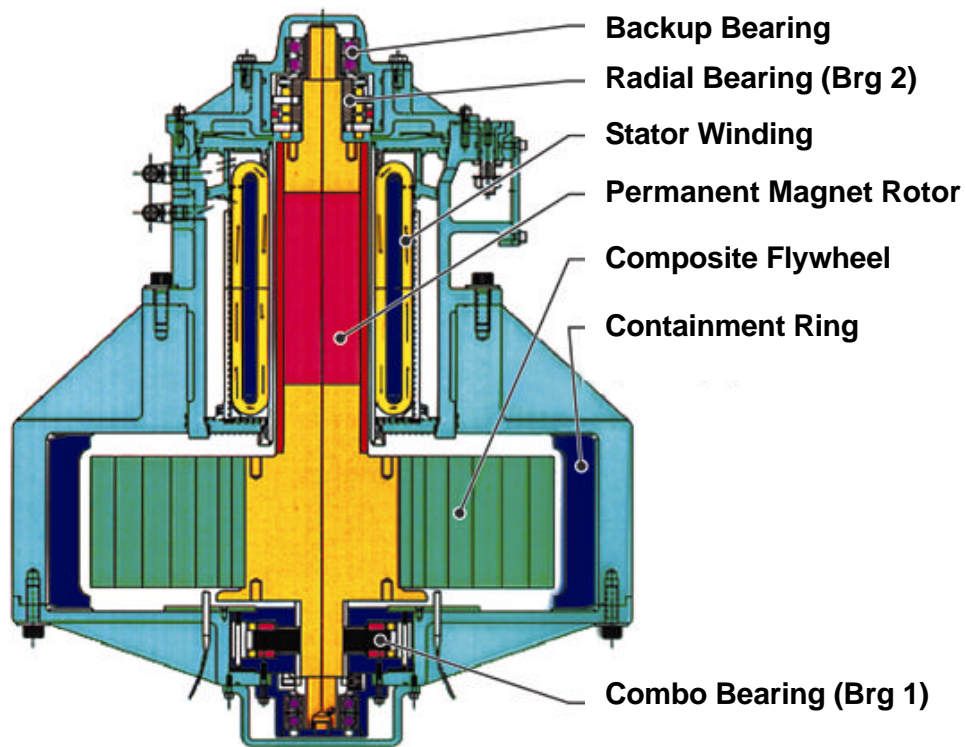


Figure 1. UT-CEM Flywheel Battery Designed for a Transit Bus.

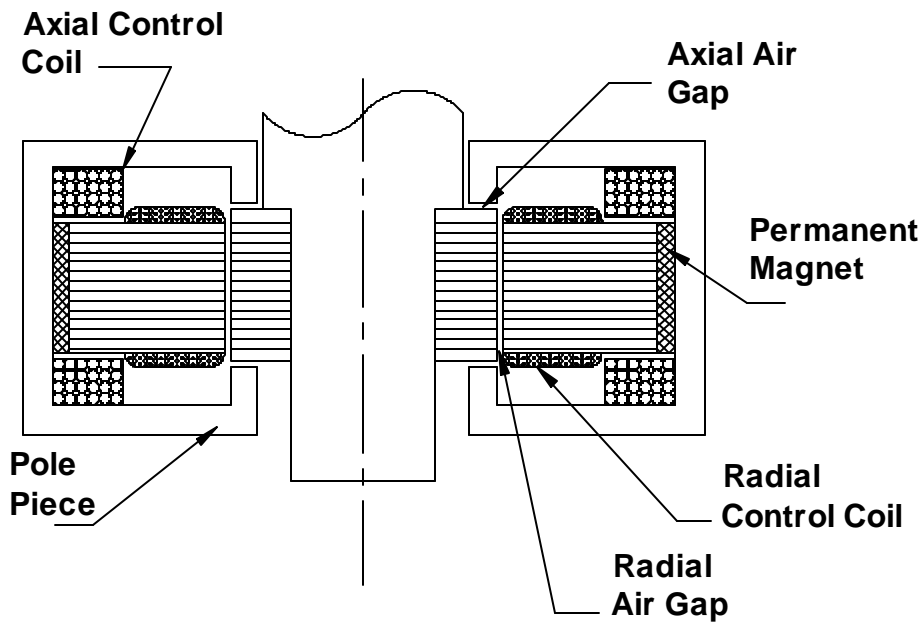


Figure 2. Combination radial/thrust permanent magnet bias bearing (Combo Bearing).

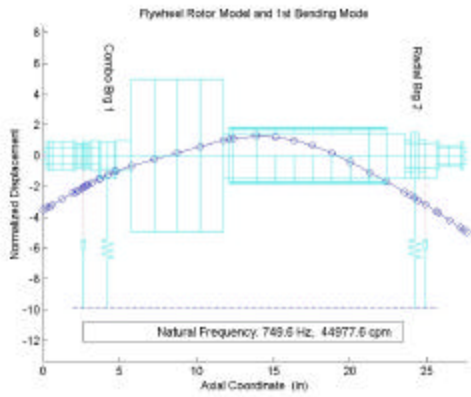


Figure 3. Rotordynamic Structural Model with First Bending Mode.

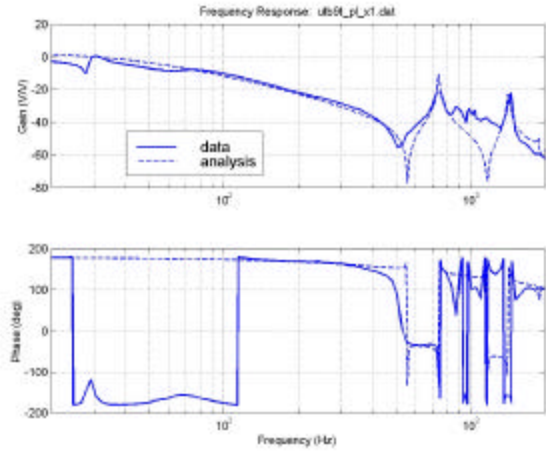


Figure 4. Predicted vs. Measured Actuator/Plant/Sensor Bode Plot (x1 axis).

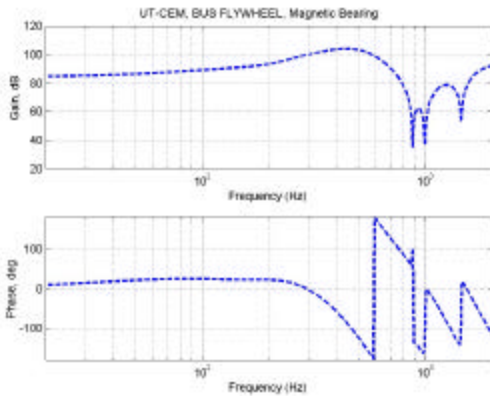


Figure 5. Single Speed SISO Mag Bearing Transfer Function, includes Sensor/Compensator/Amplifier/Actuator

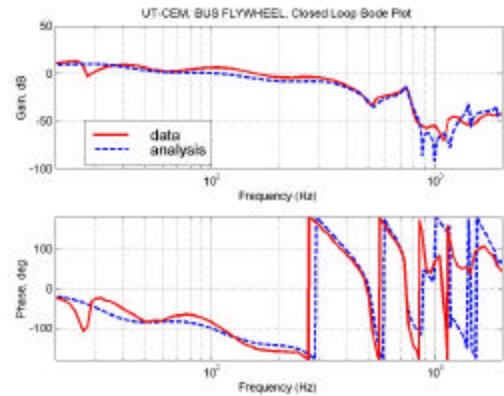


Figure 6. Predicted vs. Measured Closed Loop Bode Plot (x1 ref input, x1 sensor output).

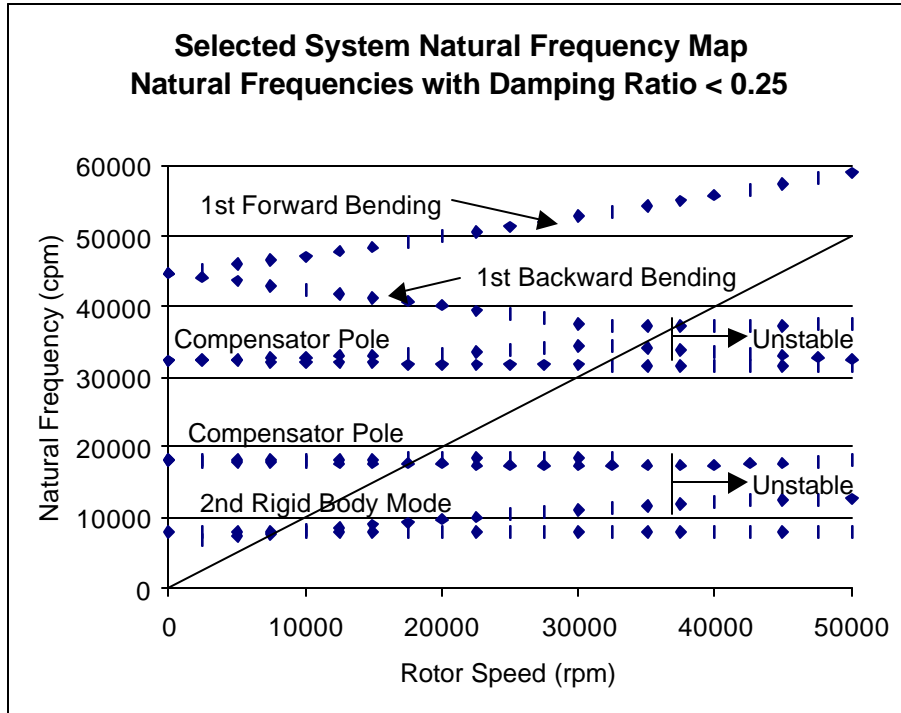


Figure 7. Selected System Natural Frequencies ( $\xi < 0.25$ ), with Speed Independent SISO Controller

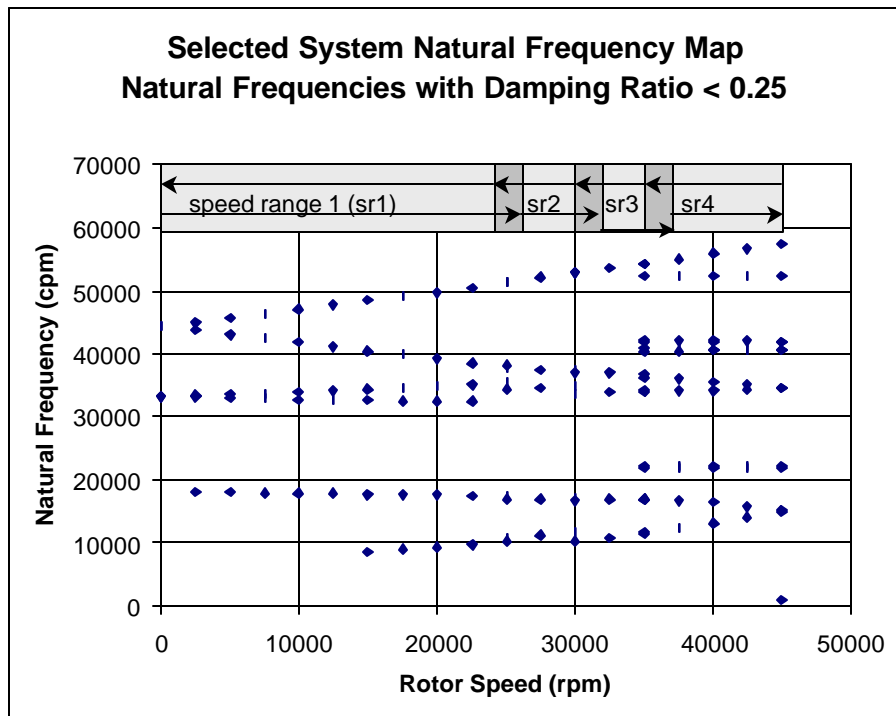


Figure 8. Selected System Natural Frequencies ( $\xi < 0.25$ ), with Gain Scheduled MIMO Controller (speed ranges shown at top).

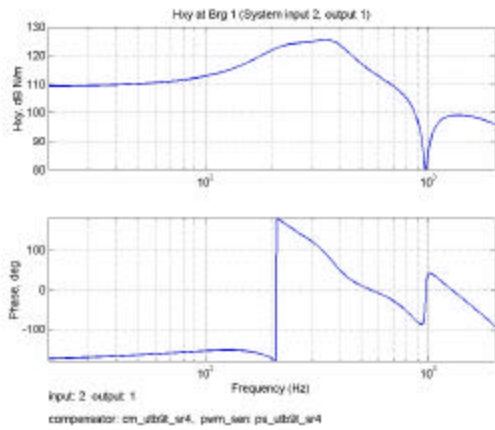


Figure 9. Hxy at Brg 1: (a) gain and phase,  
(b) Kxy and  $\omega C_{xy}$

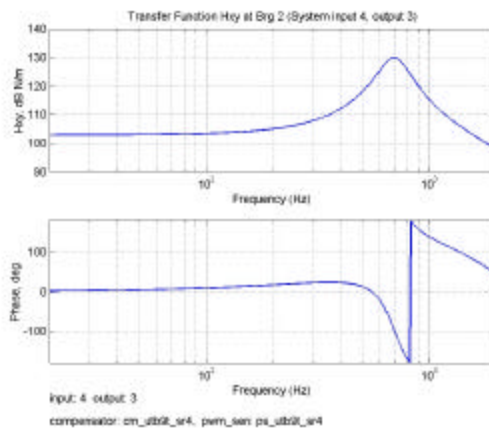


Figure 10. Hxy at Brg 2: (a) gain and phase,  
(b) Kxy and  $\omega C_{xy}$

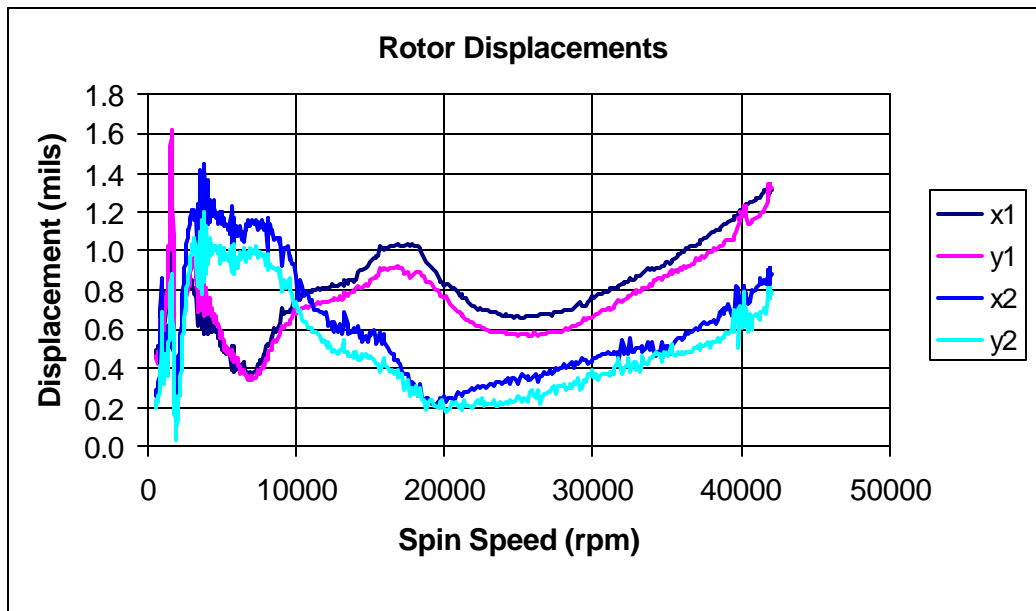


Figure 11. Synchronous Displacements during Spin Down from Full Speed

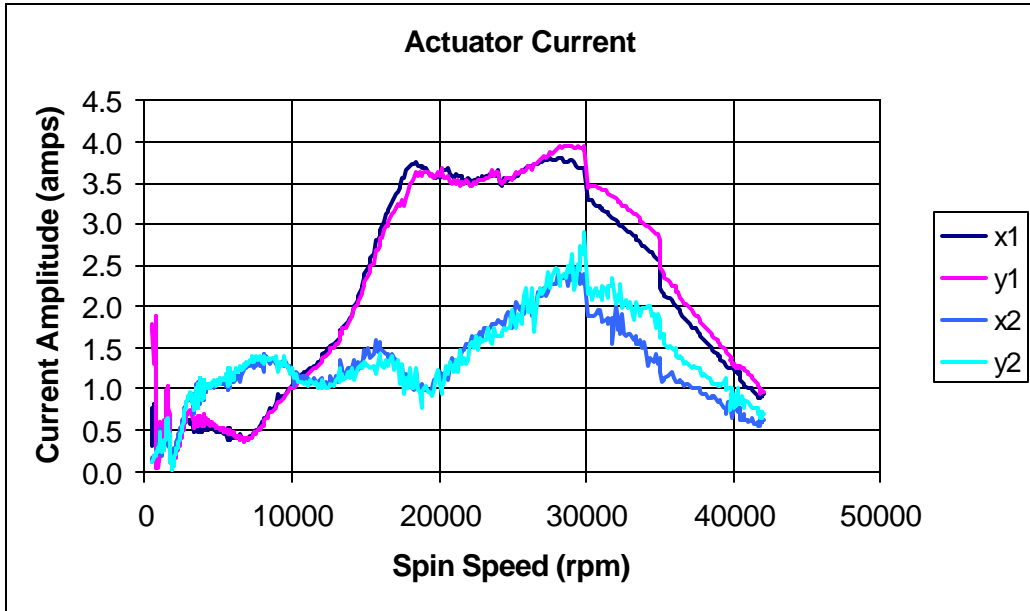


Figure 12. Synchronous Coil Current during Spin Down from Full Speed.

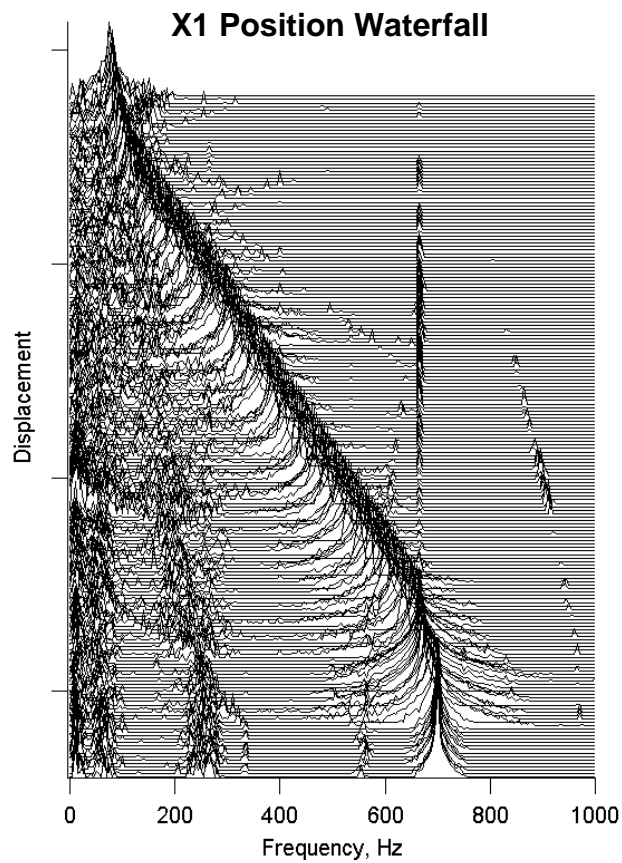


Figure 13. Waterfall plot, from x1 position sensor during spindown from 42,000 rpm to 5,000 rpm.